ADVANCED ENERGY MATERIALS
www.advenergymat.de

Highly Active $IrRuO_x/MnO_x$ Electrocatalysts with Ultralow Anode PGM Demand in Proton Exchange Membrane Electrolyzers

*Jiaqi Kang, Sebastian Möhle, Xingli Wang, Miklós Márton Kovács, Kerolus Nasser Nagi Nasralla, Johannes Schmidt, Sören Selve, Dominik Dworschak, and Peter Strasser**

Thrifting the rare iridium in proton exchange membrane water electrolyzer (PEMWE) anodes is an effective means to preempt undesired future iridium supply shortages aiding wider deployment of PEMWEs in coming years. This work explores a new family of MnO_x-supported IrO_x and $IrRuO_x$ electrocatalysts for the acidic oxygen evolution reaction (OER). Comprehensive ex situ and in situ characterization uncovers synthesis-structure-activity relationships of the OER materials with insight into the origin of their exceptional activity: The MnO_x support provides beneficial dispersion while the introduction of Ru into IrO_x/MnO_x leads to a modulation of the chemical state of Ir coupled with a strong surface reconstruction. In half-cell tests, $IrRuO_x/MnO_x$ reveals an Ir mass activity of 964.7 A g_{Ir}^{-1} at 1.53 V_{RHE}, which is 36 times higher than that of the commercial IrO_2 (C-IrO_2). It is also demonstrated that this promising catalytic OER activity translates into a realistic PEMWE performance. $IrRuO_x/MnO_x$ and IrO_x/MnO_x thin catalyst layers are developed in low Ir-loaded membrane electrode assemblies (MEAs) and an outstanding PEMWE cell performance is reported with cell voltages of 1.66 V at 2 A cm^{-2}. This translates into a favorable (Ir + Ru) platium group metal (PGM) demand of <0.05 g_{PGM} kW^{-1} at 70% voltage efficiency, meeting a 2035 technical demand target.

1. Introduction

The demand for energy rises significantly today as the world's population grows continually and economies expand.[1] This escalating demand, coupled with climate change, has spurred a renewed focus on developing new energy storage systems using environmentally friendly and more efficient energy sources. Hydrogen (H_2) is one of the most promising energy carriers today.[2] It can be produced using PEMWEs without carbon emissions by applying electricity from renewable energy sources.[3] At present, Ir-based catalysts are the state-of-the-art catalysts for OER in the anode side of PEMWEs. The development of industrially desirable Ir-based catalysts that are cost-effective, highly active, and stable is crucial for the large-scale application of PEMWEs.[4]

Various approaches are explored to meet industrial needs for active, yet low PGM OER catalysts in low PGM-loaded PEMWE anodes. Generally, Ru-based OER catalysts are more active than Ir-based catalysts. However, Ru is also a crucial PGM member and the dissolution of RuO_4 under anodic electrode potential limits the durability of Ru-rich catalysts.[5] $IrRuO_x$ mixed oxides have been widely studied and are confirmed to have good performance in MEA tests.[6] Recently, supported $IrRuO_x$ catalysts such as $IrRuO_x/TiO_2$, $IrRuO_x$/Nb-TNT, RuIr@CoNC, Ir-RuO_x@WO_3, and Ir-RuO_x@Ta_2O_5 have also been confirmed as potential candidates for OER catalysts in PEMWEs with low PGM loadings.[7] On the other hand,

J. Kang, S. Möhle, X. Wang, K. N. N. Nasralla, J. Schmidt, P. Strasser
Department of Chemistry
Technische Universität Berlin
Straße des 17. Juni 124, 10623 Berlin, Germany
E-mail: pstrasser@tu-berlin.de

The ORCID identification number(s) for the author(s) of this article can be found under https://doi.org/10.1002/aenm.202405758

DOI: 10.1002/aenm.202405758

M. M. Kovács, D. Dworschak
Helmholtz-Institut Erlangen-Nürnberg für Erneuerbare Energien (IET-2)
Forschungszentrum Jülich GmbH
Cauerstraße 1, 91058 Erlangen, Germany

M. M. Kovács
Department of Chemical and Biological Engineering
Friedrich-Alexander-Universität Erlangen-Nürnberg
Immerwahrstraße 2a, 91058 Erlangen, Germany

S. Selve
Center for Electron Microscopy (ZELMI)
Technische Universität Berlin
Straße des 17. Juni 135, 10623 Berlin, Germany

MnO_x among non-PGM metals features an acidic stability up to 1.5 V_{RHE} at pH = 1, which is considered one of the most promising non-PGM metals that may be a substitute for PGM-based OER catalysts.[8] Some previous studies have indicated that it might have a similar reaction mechanism to IrO_x.[9] However, the stability and activity of PGM-free MnO_x catalysts have been poor, even compared to low-content Ir catalysts. This led to research on $IrMnO_x$ mixed oxides, which exhibited a synergistic effect, leading to improved electrochemical behavior.[10] Other recent studies focused on loading pure Ir or Ru nanoparticles onto MnO_2 to achieve OER activity at ultralow noble metal loadings (<10 wt.%).[11] These noble metals are believed to help stabilize MnO_x somewhat under acidic conditions, however, a demonstration of this effect is missing, as acidic OER catalysts with ultralow noble metal loadings have notoriously been facing stability problems and low conductivity. From these earlier works, supporting $IrRuO_x$ mixed metal oxides on nanostructured MnO_x emerges as a novel and effective strategy toward catalyst/support couples with excellent OER activity and acceptable MnO_x support stability while thrifting Ir.

Herein, we report the new family of $IrRuO_x/MnO_x$ OER catalysts for acidic environments. Ir and Ru precursors were loaded onto MnO_x using an ion exchange method. Powder X-ray diffraction (XRD) patterns and energy-dispersive X-ray spectroscopy (EDX) mappings from transmission electron microscopy (TEM) confirmed that Ir and Ru are homogeneously dispersed on MnO_x, while Ir and Ru form separated-phased $IrRuO_x$. X-ray photoemission spectroscopy (XPS) and X-ray absorption spectroscopy (XAS) were conducted to investigate the electronic structure of these materials. The oxidation state of Ir in $IrRuO_x/MnO_x$ was found to be higher than that in the standard due to the participation of Ru. Also, in situ XAS revealed that $IrRuO_x/MnO_x$ supports a distinctly different catalytic reaction mechanism compared to the IrO_x/MnO_x. Strong surface reconstruction during OER led to high activity. Rotating disk electrode (RDE) results confirmed that $IrRuO_x/MnO_x$ had superior electrochemical performance. Scanning flow cell inductively coupled mass spectrometry (SFC-ICP-MS) indicated that Ru on the surface, on the one hand, protected against the initial dissolution of Ir and Mn when inserted in the electrolyte, and on the other hand, it will dissolve during the reaction, which induced surface reconstruction. Both IrO_x/MnO_x and $IrRuO_x/MnO_x$ showed excellent performance in MEA measurements, achieving 3 A cm^{-2} at 1.7 V. The power-specific PGM loading at 70% lower heating value (LHV) (≈1.79 V) was 0.04 g_{Ir} kW^{-1}, which exceeds the 2035 target.[4,12]

2. Results and Discussion

2.1. Synthesis and Characterizations

A set of 9 MnO_x-supported IrO_x/MnO_x, RuO_x/MnO_x, and $IrRuO_x/MnO_x$ was synthesized using aqueous ion exchange as illustrated in **Figure 1a**. First, a MnO_x-AP (AP for "used as-prepared") support material was prepared using a customized hydrothermal method. Subsequently, the MnO_x-AP material along with varying stoichiometric amounts of Ir and Ru precursors were slowly added to an ambient-pressure reflux synthesis reactor under stirring. After reacting for 12 h at 95 °C, the obtained materials were annealed at 350 °C in air using a static tube furnace. For comparison, MnO_x was synthesized by directly annealing the MnO_x-AP at 350 °C in air. Detailed synthesis procedures are provided in the Supporting Information. The final Ir and Ru loadings were determined using X-ray fluorescence (XRF) spectroscopy, resulting in an Ir content of 14–65 wt.% for IrO_x/MnO_x and a PGM loading of 40–50 wt.% for $IrRuO_x/MnO_x$. The Ir to Ru ratio was 2.15 for $IrRuO_x/MnO_x$ based on XRF. The resulting atomic Ir:Ru: Mn ratio was 28:18:59, which justified that MnO_x acted as a support. Detailed elemental loadings and atomic ratios are listed in Table S1 (Supporting Information).

The morphologies of the synthesized catalysts were investigated using scanning transmission electron microscopy (STEM). STEM images (Figure S1, Supporting Information) revealed a porous structure composed of small, needle-like dendrites typical of α-MnO_2. The low crystallinity of the α-MnO_x structure was further confirmed by XRD (Figure S2a, Supporting Information). High-resolution TEM (HRTEM) images of the catalysts are shown in Figure 1b,c. Dark particles, ≈1 nm in size, observed on the MnO_x substrates were identified as $Ir(Ru)O_x$ mixed oxide. PGM mixed oxide particle sizes in $IrRuO_x/MnO_x$ were slightly larger than those in IrO_x/MnO_x (Figure S3a,b, Supporting Information), yet smaller than those of RuO_x/MnO_x (Figure S3c, Supporting Information). Selected area diffraction (SAED) analysis of $IrRuO_x/MnO_x$ and IrO_x/MnO_x catalysts indicated that both have rather amorphous structures (Figure S4, Supporting Information). XRD patterns in Figure 1d provide evidence that IrO_x, RuO_x, and $IrRuO_x$ feature distinct Bragg reflections compared to the MnO_x support. Figure S2d (Supporting Information) presents the XRD patterns within the 10° to 80° range. Negligible Bragg peak shifts between pure MnO_x and the $IrRuO_x/MnO_x$ and IrO_x/MnO_x catalysts confirmed that MnO_x was present as a separate phase and, hence, primarily acted as a support rather than forming mixed oxide phases. Broad IrO_x peaks suggested the formation of rather amorphous IrO_x phases on the surface of MnO_x, with peak intensity increasing with higher Ir loadings (Figure S1b, Supporting Information). When Ru was introduced in the catalyst, the Bragg peak ≈28°, representing the (110) facets of the rutile IrO_2 and RuO_2, became significantly more pronounced. This suggested that Ru was conducive to a higher crystallinity, preferred orientation, and larger crystallite size of the $IrRuO_x$ phase. The peak position was similar to that of the (110) facet position in commercial $IrRuO_x$ (C-$IrRuO_x$), but it shifted to lower Bragg angles compared to the (110) peak in RuO_x/MnO_x due to lattice expansion from Ir incorporation.[6a] XRD and EDX mappings across different areas (Table S2, Supporting Information) further confirmed that Ir and Ru formed distinct $IrRuO_x$ phases located on MnO_x. High-angle annular dark-field (HAADF) TEM images and corresponding elemental mappings (Figure 1e,f; EDX spectra in Figure S5, Supporting Information) clearly show that Ir and Ru were homogeneously dispersed on MnO_x, providing high coverage of the catalyst support. The amorphous MnO_x provides an abundance of defects and hydroxide groups on its surface, facilitating the bonding of Ir/Ru atoms to substrates through ion exchange. These initially bonded Ir/Ru atoms act as nucleation seeds, leading to the formation of a large number of ultra-small amorphous $IrRuO_x$ particles. The immobilization resulting from the bonding between Ir/Ru and O on the MnO_x surface through ion exchange also promotes the homogeneous dispersion of $IrRuO_x$ particles.[7c,f,13]

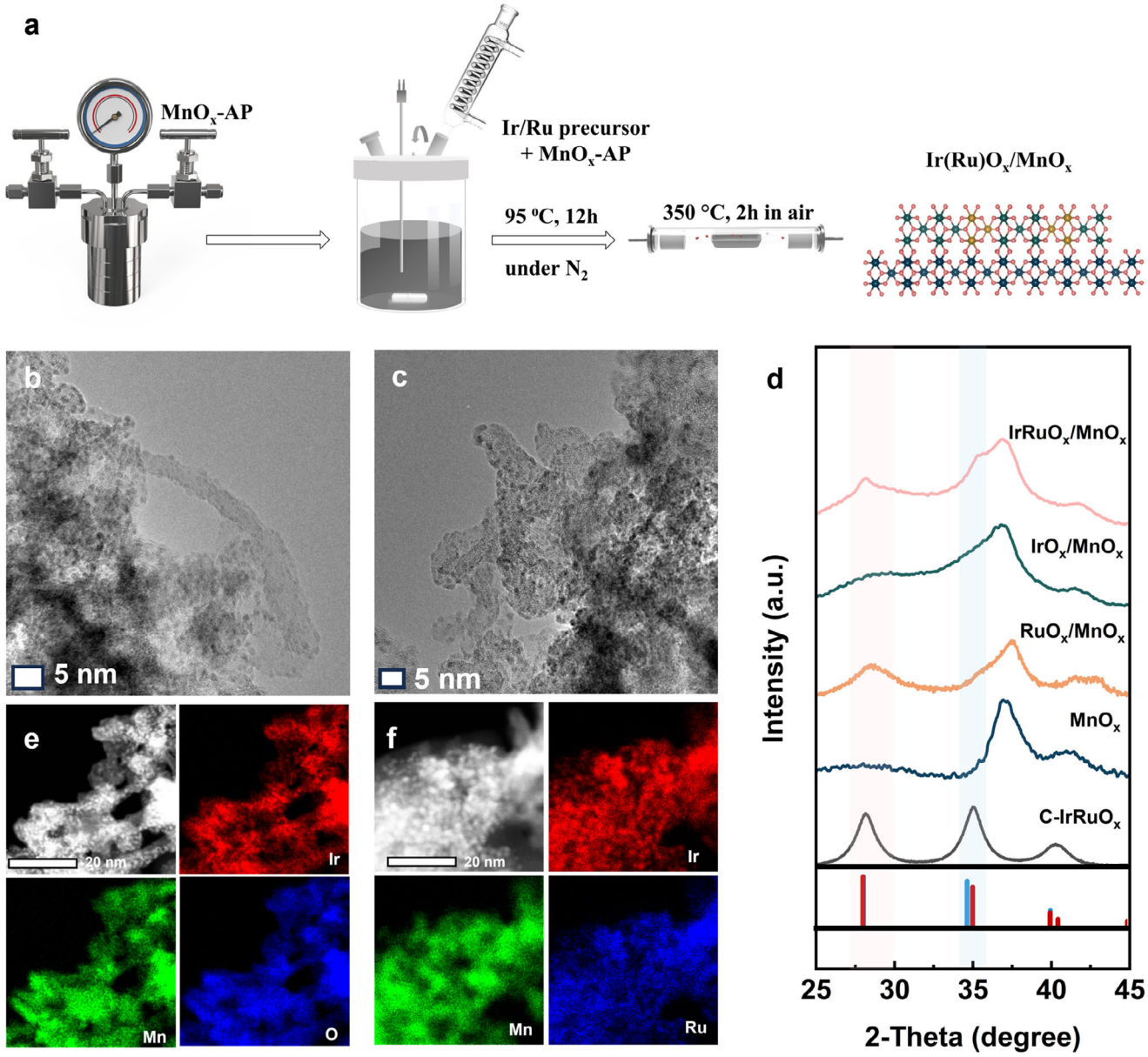

Figure 1. Synthesis and structural characterization of IrO_x/MnO_x and $IrRuO_x/MnO_x$. a) Schematic of the synthesis route. b) HRTEM image of IrO_x/MnO_x. c) HRTEM image of $IrRuO_x/MnO_x$. d) XRD patterns. The red reference pattern refers to standard IrO_2 (PDF#15-0870), and the blue reference pattern refers to RuO_2 (PDF#43-1027). Pink and blue shadows show the 2-theta regions of (110) and (101) of rutile IrO_2 and RuO_2. e) Elemental mapping of IrO_x/MnO_x. f) Elemental mapping of $IrRuO_x/MnO_x$. For (e), upper left: HAADF, lower left: Mn-map, upper right: Ir-map, lower right: O-map. For f), upper left: HAADF, lower left: Mn-map, upper right: Ir-map, lower right: Ru-map.

2.2. Electronic Structures

To further investigate the electronic structures of IrO_x/MnO_x and $IrRuO_x/MnO_x$, XAS and XPS measurements were conducted. **Figure** 2a displays the X-ray absorption near-edge structure (XANES) spectra of both catalysts and reference materials at Ir L_3-edge. The white-line peak energy positions of both catalysts are similar to that of C-IrO_2 with higher intensity, indicating higher valence states of Ir in these two catalysts due to the participation of Mn. The white-line peak energy shift of $IrRuO_x/MnO_x$ related to that of IrO_x/MnO_x is similar to the shift between C-$IrRuO_x$ and C-IrO_2. This shift is attributed to the incorporation of Ru, which alters the electronic structure of IrO_x. Figure 2b shows XPS spectra in the Ir 4f region. The Ir $4f_{7/2}$ peak position of rutile C-IrO_2 was 62 eV (Ir^{4+}), while that of IrO_x/MnO_x was at 61.9 eV and that of $IrRuO_x/MnO_x$ was at 62.1 eV (Table S3, Supporting Information), indicating a similar Ir oxidation state of ≈4 in all samples. The Fourier transform of extended X-ray absorption fine structure (FT-EXAFS) spectra at the Ir L_3-edge are shown in Figure 2c, with the corresponding k^2-weighted EXAFS spectra and simulation results are shown in Figure S6 and Table S4 (Supporting Information). Since the IrO_2 and RuO_2 have

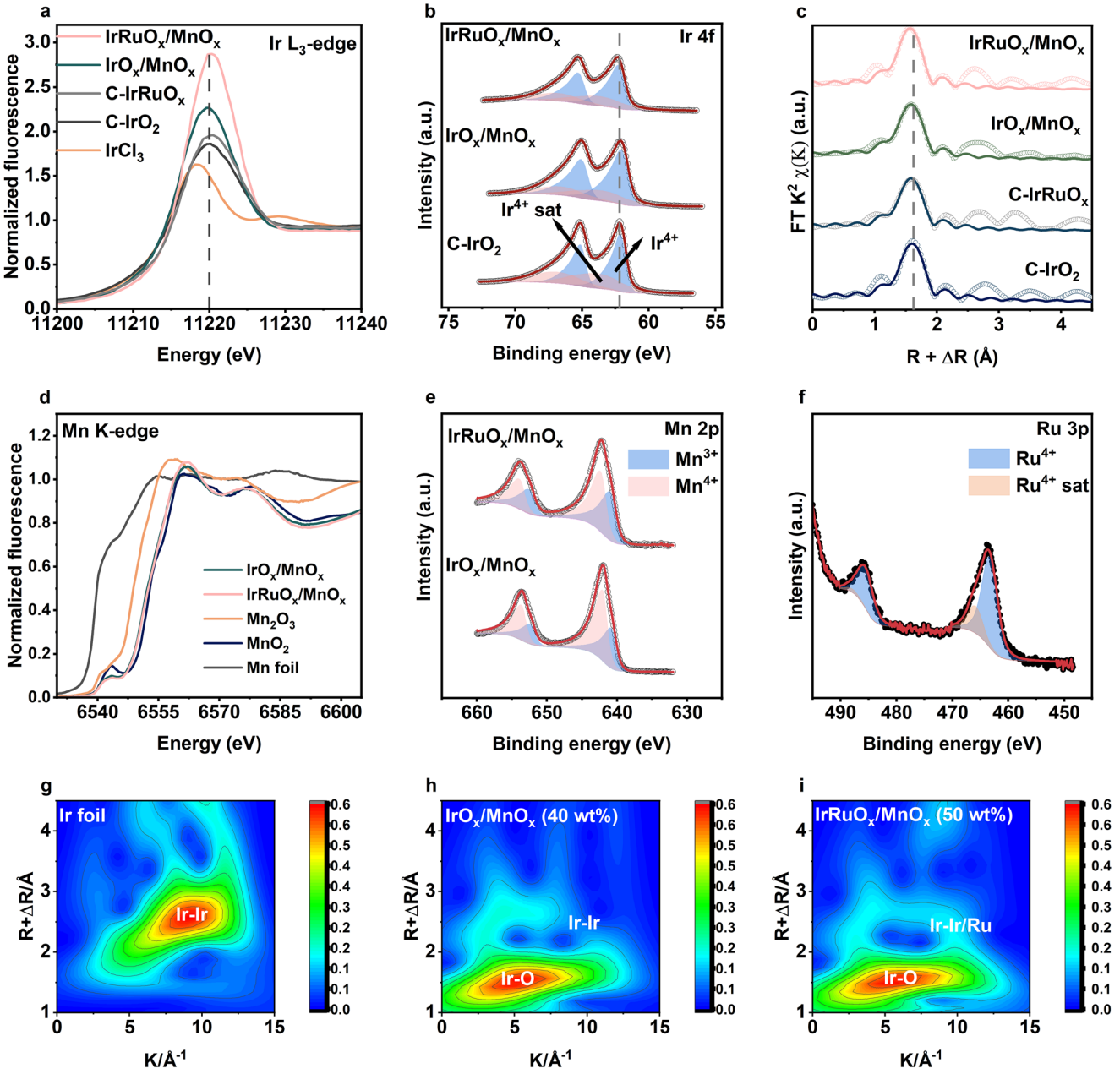

Figure 2. X-ray spectra characterization of the electronic structures of IrO$_x$/MnO$_x$ and IrRuO$_x$/MnO$_x$. a) XANES spectra at the Ir L$_3$-edge of IrO$_x$/MnO$_x$, IrRuO$_x$/MnO$_x$, C-IrO$_2$, C-IrRuO$_x$, and IrCl$_3$. b) XPS spectra of Ir 4f. c) FT-EXAFS oscillations at the Ir L$_3$-edge. d) XANES spectra at the Mn K-edge. e) XPS spectra of Mn 2p. f) XPS spectrum of Ru 3p. g) WT-EXAFS for Ir foil. h) WT-EXAFS for IrO$_x$/MnO$_x$ with an Ir loading of 40 wt.%. And i) WT-EXAFS for IrRuO$_x$/MnO$_x$ with an Ir loading of 40 wt.%.

very similar crystal structures, the structure change was negligible in FT-EXAFS spectra. IrRuO$_x$/MnO$_x$ exhibited a shorter Ir—O bond length of 1.97 Å compared to IrO$_x$/MnO$_x$ (1.98 Å), suggesting a change in chemical states due to the incorporation of Ru as shown in Figure 2a. A similar bond length difference was observed between C-IrO$_2$ (1.99 Å) and C-IrRuO$_x$ (1.98 Å). Both supported catalysts showed shorter Ir—O bond lengths compared to C-IrO$_2$ (Table S4, Supporting Information). This slightly shorter Ir—O bond length indicates a more stable Ir(Ru)O$_x$ structure, which might be related to a compressive strain effect induced by the presence of a short Mn—O bond. Figure 2d shows the XANES spectra in Mn K-edge, revealing that bulk Mn in all catalysts had an oxidation state near Mn^{4+}. However, XPS spectra of Mn 2p in Figure 2e indicate that Mn exists in a mixed oxidation state of Mn^{3+} and Mn^{4+} (see XPS data in Table S5, Supporting Information). Since XPS is a surface-sensitive technique, we can interpret that Mn^{3+} is present on the surface rather than in the bulk. The XANES spectrum of MnO$_x$-AP also shows an oxidation state lower than 4 (Figure S7, Supporting Information), The large Mn^{3+}-to-Mn^{4+} ratio on the surface of IrO$_x$/MnO$_x$

and $IrRuO_x/MnO_x$ compared to pure MnO_x is attributed to the presence of the $Ir(Ru)O_x$ phases on the surface (Figure S8, Supporting Information). Apparently, it limited the further oxidation of Mn in MnO_x-AP to a higher oxidation state and induced changes in the valence states of Ir. It can also explain the higher OH-to-O surface hydroxylation ratios in all catalysts compared to the pure MnO_x (Figure S9, Supporting Information). The XPS spectrum of Ru 3p is exhibited in Figure 2f. The peak position of Ru $3p_{3/2}$ is at 463.3 eV, indicating an oxidation state of 4. Ru 3d spectrum confirmed the same results (Figure S8b, Supporting Information). To verify the formation of Ir—Ru bonds, we synthesized 40 wt.% IrO_x/MnO_x matching the Ir loading of $IrRuO_x/MnO_x$ and performed wavelet transform (WT) analysis on the EXAFS data. Figure 2g shows the WT-EXAFS spectrum of Ir foil. The peak of the Ir—Ir bond is located at high k regions (≈10 $Å^{-1}$), whereas the Ir—O bond signal in rutile IrO_2 is found at low k regions (≈5 $Å^{-1}$) (Figure S10a, Supporting Information). IrO_x/MnO_x with the same Ir loading as $IrRuO_x/MnO_x$ (40 wt.%) exhibits a weak Ir—Ir bond intensity (Figure 2h). However, after adding Ru, the intensity in the Ir-metal k-regions increased (Figure 2i). This indicated the formation of Ir—Ru bonds, which behave similarly to the Ir—Ir bond. This conclusion is supported by our finding that increasing the Ir loading from 40 to 50 wt.% also enhanced the intensity of the Ir-M signal in the very same WT region (see label in Figure S10b, Supporting Information). The WT-EXAFS spectra at the Mn K-edge in Figure S11 (Supporting Information) show the formation of Mn-O-Ir/Mn-O-Ru, consistent with the ion exchange mechanism and supporting the previous hypothesis regarding the compressive strain-induced change in the Ir—O bond.[14]

2.3. Catalytic Activity and Stability in Acidic Liquid Electrolyte

The electrochemical performance of $IrRuO_x/MnO_x$, IrO_x/MnO_x, RuO_x/MnO_x, MnO_x, and commercial catalysts were first evaluated using RDE and SFC-ICP-MS. Prior to these catalytic tests, the impact of the Ir weight loadings of IrO_x/MnO_x on its conductivity and OER activity was explored (Figures S12 and S13, Supporting Information). This helped determine the most suitable Ir loading for optimal MEA tests. To optimize Ir loadings, bulk conductivity and RDE measurements were performed. When the Ir loading exceeded 30 wt.%, IrO_x/MnO_x showed a resistivity below 1 Ω cm, making it suitable for PEMWE tests.[15] IrO_x/MnO_x with an Ir loading of 50 wt.% was chosen as it showed the lowest OER overpotential at 10 mA cm^{-2}. An identical total (Ir + Ru) PGM loading was adopted and applied to $IrRuO_x/MnO_x$ for comparison. As shown in **Figure 3**a, $IrRuO_x/MnO_x$, RuO_x/MnO_x, and IrO_x/MnO_x exhibited significantly higher OER activity compared to the two commercial catalysts. MnO_x itself showed only low OER catalytic activity at high potentials. Although MnO_x primarily acted as a support, it may also partially contribute to catalyzing oxygen evolution. $IrRuO_x/MnO_x$ had an overpotential of 256 mV at 10 mA cm^{-2}, whereas IrO_x/MnO_x exhibited an overpotential of 294 mV. Although RuO_x/MnO_x showed a superior overpotential of 254 mV, its rapid degradation due to Ru dissolution during the accelerated stress test (AST) indicated that RuO_x/MnO_x was not suitable for PEMWE cell tests (Figure 3b). $IrRuO_x/MnO_x$ demonstrated a mass activity (MA) of 964.7 A g_{Ir+Ru}^{-1} at 1.53 V_{RHE}, which was over seven times higher than that of C-$IrRuO_x$ and 36 times higher than that of C-IrO_2. Even after 5000 AST cycles, it retained an MA of 267.1 A g_{Ir}^{-1}. The remaining MA after AST was 28% for $IrRuO_x/MnO_x$ and 30% for IrO_x/MnO_x, both of which were higher than those of C-$IrRuO_x$ and C-IrO_2. The significant increase in activity for the supported catalysts could be attributed to the introduction of MnO_x. Additionally, the twofold increase in MA of $IrRuO_x/MnO_x$ compared to IrO_x/MnO_x even after AST, may be related to the electronic structure changes by introducing Ru. Figure 3c shows the Tafel plots. IrO_x/MnO_x had a Tafel slope of 48.5 mV dec^{-1}, which is lower than $IrRuO_x/MnO_x$ (62.1 mV dec^{-1}), suggesting that the two catalysts may have different kinetic mechanisms. Cyclic voltammetry (CV) revealed that the $IrRuO_x/MnO_x$ and IrO_x/MnO_x exhibited typical amorphous IrO_x features (Figure S14a, Supporting Information). The trend in electrochemical surface area (ECSA) was evaluated using the proxy value of double layer capacitances calculated from the current at different scan rates (Figures S14b,c and S15, Supporting Information). IrO_x/MnO_x had a slightly larger ECSA compared to $IrRuO_x/MnO_x$, consistent with smaller particles. Both IrO_x/MnO_x and $IrRuO_x/MnO_x$ exhibited much larger ECSAs compared to C-IrO_2 and C-$IrRuO_x$ due to the support effect of MnO_x. The spider diagram in Figure 3d summarizes the key parameters of investigated catalysts. In addition to the above-mentioned properties, resistivity was also taken into consideration, while all catalysts remained below 1 Ωcm range. C-$IrRuO_x$ showed lower resistivity compared to C-IrO_2, and a similar trend was found for IrO_x/MnO_x and $IrRuO_x/MnO_x$ (Figure S16, Supporting Information). Overall, the spider diagram analysis confirms that $IrRuO_x/MnO_x$ is a very promising candidate as an OER catalyst based on the screening in an ideal environment.

Additionally, SFC-ICP-MS measurements were performed to test the stability and dissolution of metallic catalyst components. As shown in Figure 3e, when the catalysts were immersed in electrolyte at 1.1 V_{RHE}, Mn in IrO_x/MnO_x showed a stronger initial dissolution than the binary $IrRuO_x/MnO_x$ catalyst. Generally, we attribute the dissolution of MnO_x to the presence of Mn^{3+} near the surface as evidenced by XPS (Figure 2e). The dissolution of Mn appears similar to that of Ir in the two catalysts, but in a larger amount (Figure 3e bottom). Interestingly, the dissolution rates of Ir and Mn in $IrRuO_x/MnO_x$ were much lower than those in IrO_x/MnO_x. Also, Ru exhibited negligible dissolution at 1.1 V_{RHE} when the catalyst was first conducted with electrolyte. This could be related to the higher crystallinity of $IrRuO_x$ compared to IrO_x, forming a protective layer that prevents Mn dissolution (Figure 1d). In order to calculate stability numbers (S-numbers) under OER, we held the current at 1 mA cm^{-2} for 600s. Mn dissolution was minimal under OER conditions. The dissolution rate of Ru was much higher than that of Ir, consistent with previous reports.[16] The S-number of Ir in IrO_x/MnO_x was similar to that of reported hydrous IrO_x (10^4),[17] while the S-number for Ir in $IrRuO_x/MnO_x$ was higher than that in IrO_x/MnO_x. If both Ir and Ru were considered in calculating the S-number for $IrRuO_x/MnO_x$, the S-number dramatically decreased to 10^3 (Figure S17 and Table S7, Supporting Information). This suggests that Ru was the initially more active catalytic species. As a consequence, it could lead to dissolution-induced surface reconstruction and alter the reaction mechanism on the surface.[18]

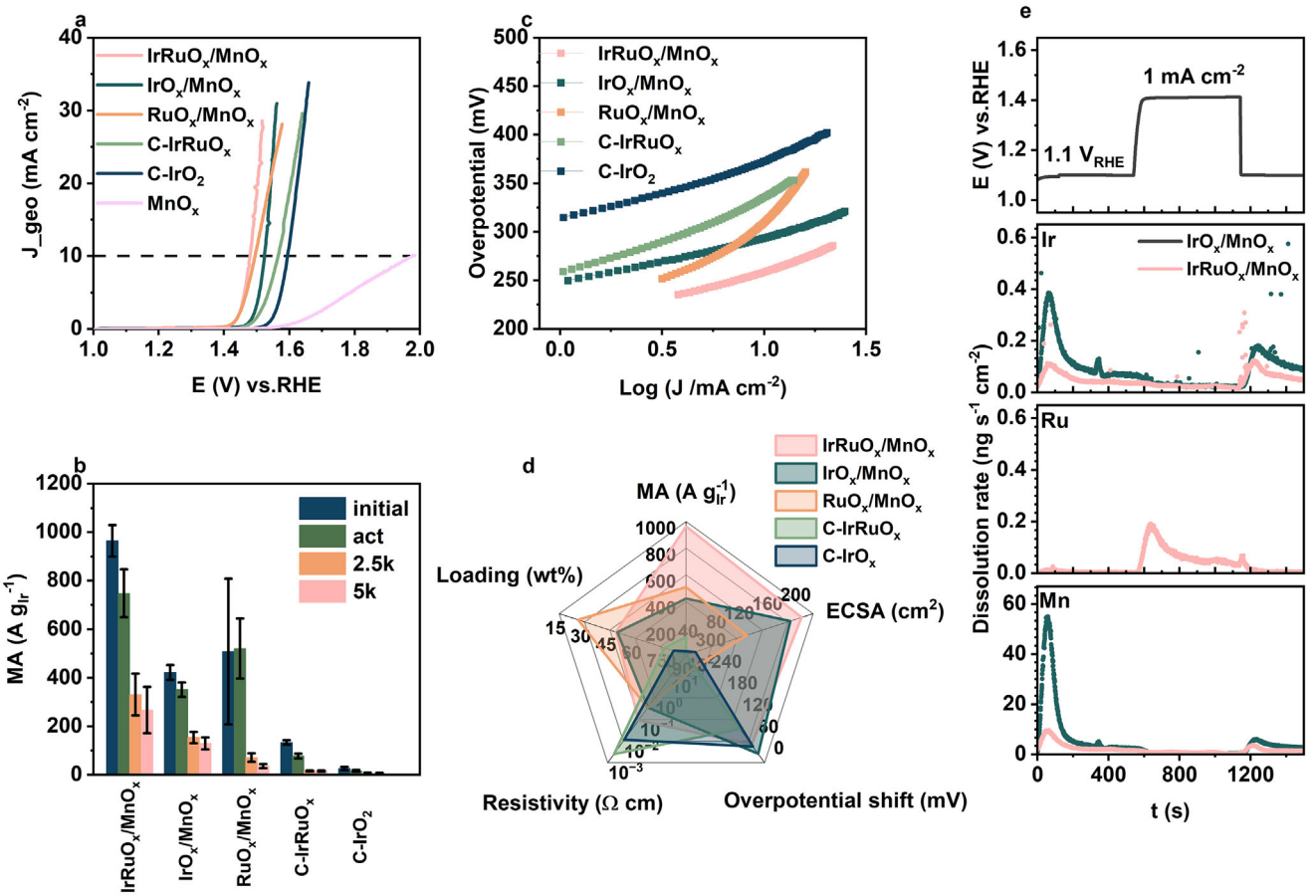

Figure 3. Electrochemical performance. a) Polarization curves of as-prepared samples. b) MA changes during AST at 1.53 V_{RHE}. c) Tafel plots. d) Spider diagram depicting the correlations of electrochemical and physical properties. e) Dissolution profiles of different elements in IrO_x/MnO_x and $IrRuO_x/MnO_x$ determined by SFC-ICP-MS at 1.1 V_{RHE} and at 1 mA cm^{-2}. Applied electrochemical profiles (top) and experimental online dissolution rates of Ir (second from the top), Ru (second from the bottom), and Mn (bottom). All RDE results are iR compensated and the measurements are performed in N_2-saturated 0.05 M H_2SO_4 electrolyte. (Ir + Ru) PGM loading on the gold electrode is 30 μg_{Ir+Ru} cm^2. SFC-ICP-MS measurements are performed in Ar-saturated 0.1 M $HClO_4$. (Ir + Ru) PGM loading is 10 μg_{Ir+Ru} cm^2.

2.4. In Situ XAS Measurements

In situ XAS measurements were performed at the Ir L_3-edge in **Figure 4**. The upper potential of $IrRuO_x/MnO_x$ was set to 1.5 V_{RHE} rather than 1.55 V_{RHE} due to the high catalyst activity and resulting bubble formation. The OER current began at 1.5 V_{RHE}. Figure 4a exhibits the XANES spectra of IrO_x/MnO_x at different applied potentials. The spectra remained essentially unchanged as the potential increased from 1.2 to 1.55 V_{RHE} and back, indicating a stable chemical state of Ir in IrO_x/MnO_x. By contrast, the in situ XANES spectra of $IrRuO_x/MnO_x$ in Figure 4c showed a reversible shift to higher energy under OER potentials, and the white line peak intensity decreased at 1.5 V_{RHE}. This phenomenon may be induced by the formation of the increased Ir-Ir interaction (peak between 2 and 3 Å in Figure 4d), which can be attributed to the removal of oxygen from the lattice.[19] Figure S18 (Supporting Information) displays the in situ XANES spectra of these two catalysts at the Mn K-edge. The chemical state of Mn showed a similar trend to Ir. The Mn oxidation state increased with electric potential only for the $IrRuO_x/MnO_x$. Previous papers have reported that Mn might share a similar OER mechanism with Ir and could also partially contribute to the catalytic process. Additionally, the dissolution of Ru may induce an increase in the oxidation state of Mn in MnO_x.

To further reveal the electronic structural changes during OER, FT-EXAFS data of both catalysts were analyzed. The EXAFS spectra are presented in Figures S19 and S20 (Supporting Information). The related simulation parameters are listed in Table S8 (Supporting Information). The FT-EXAFS oscillations of IrO_x/MnO_x at Ir L_3-edge in Figure 4b showed negligible changes with increasing potentials. The Ir—O bond length was 1.98 Å and remained the same between 1.2 and 1.55 V_{RHE}. By contrast, the FT-EXAFS oscillations of $IrRuO_x/MnO_x$ (Figure 4d) revealed significant changes as the potential increased. Simulations reveal that the bond length of Ir-O decreased from 1.99 Å at 1.2 V_{RHE} to 1.96 Å at 1.5 V_{RHE}, indicating an increase of the oxidation state of Ir (higher than Ir^{4+} during OER) in the catalyst and substantial structural rearrangement during OER. This change in the chemical state of Ir appears consistent with the Ru dissolution from Figure 3e at 1.5 V_{RHE}. Combined with SFC-ICP-MS results, we conclude the presence of a Ru dissolution-induced reconstruction. Previous studies have demonstrated that strong

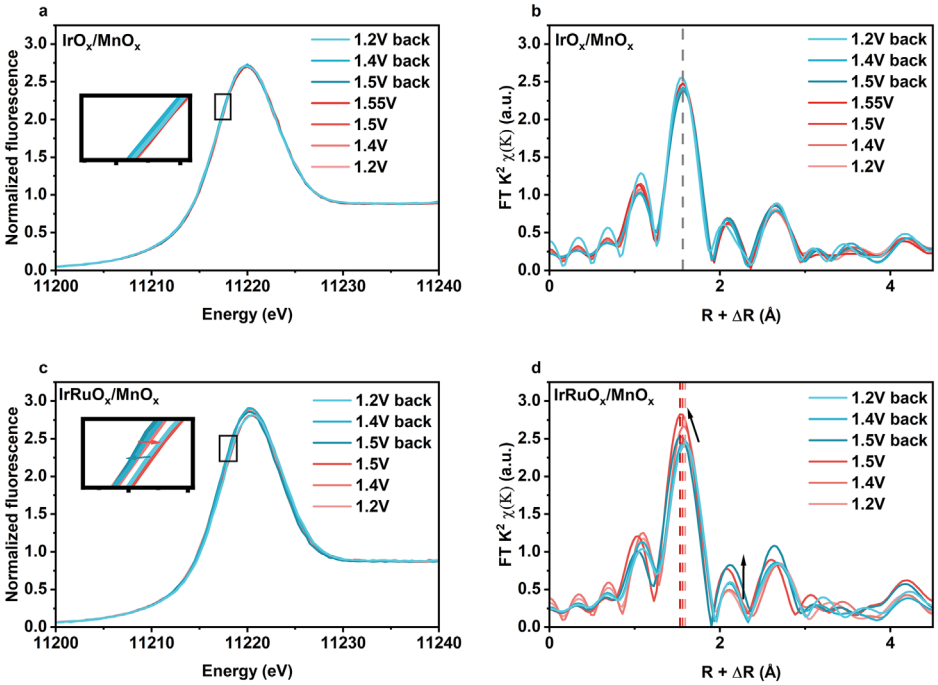

Figure 4. In situ XAS measurements at the Ir L_3-edge at different applied potentials. a) XANES spectra of IrO_x/MnO_x at different applied potentials from 1.2 to 1.55 V_{RHE} and back. b) Corresponding k^2-weighted FT-EXAFS patterns of IrO_x/MnO_x. c) XANES spectra of $IrRuO_x/MnO_x$ at different applied potentials from 1.2 to 1.5 V_{RHE} and back. d) Corresponding k^2-weighted FT-EXAFS patterns of $IrRuO_x/MnO_x$.

surface rearrangements are associated with improved Ir dissolution stability, which aligns with the SFC-ICP-MS data, as Ir had a higher S number in $IrRuO_x/MnO_x$.[19] Additionally, the FT-EXAFS oscillations of $IrRuO_x/MnO_x$ at the Mn K-edge showed significant structural rearrangement as well (Figure S21b, Supporting Information). The differences in in situ XAS spectra between IrO_x/MnO_x and $IrRuO_x/MnO_x$ imply that the initial dominant metallic compound for OER in these two catalysts is different (Ru vs Ir). This may have consequences for the OER. As Ru in $IrRuO_x/MnO_x$ dissolves under OER conditions, it creates lattice defects in the structure with metal vacancies favoring the lattice oxygen evolution mechanism (LOM). Tetramethylammonium cations (TMA^+) can interact with O_2^{2-}, a key species involved in LOM. The decrease in the activity of $IrRuO_x/MnO_x$ in the presence of TMAOH in the electrolyte, as shown in Figure S22 (Supporting Information), provides further evidence for the occurrence of the LOM.[20] Comparable competitive relationships between LOM and the alternative adsorbate evolution mechanism (AEM) have previously been reported for $IrRuO_x$ and defect-rich IrO_2/RuO_2.[18a,21] Catalysts undergoing LOM generally exhibit larger chemical state changes compared to those following the AEM, which contributes to their high OER activity.

2.5. MEA Measurements

Single-cell PEMWE tests were carried out in order to test the IrO_x/MnO_x and $IrRuO_x/MnO_x$ under realistic electrocatalytic OER conditions. MEAs were prepared using a decal transfer method and tested using a commercial test station at 80 °C under ambient pressure. The detailed cell setup is illustrated in Figure S23 (Supporting Information). **Figure 5a** presents the polarization curves of IrO_x/MnO_x, and $IrRuO_x/MnO_x$ compared to a commercial benchmark catalyst (Umicore). The polarization curve of the benchmark with lower geometric Ir loading (0.47 mg_{Ir} cm^{-2}) is shown in Figure S24 (Supporting Information) for comparison. It is evident that $IrRuO_x/MnO_x$ (0.24 mg_{Ir} cm^{-2}) and IrO_x/MnO_x (0.26 mg_{Ir} cm^{-2}) exhibited higher hydrogen production activity compared to the benchmark catalyst. The high-frequency resistances (HFRs) in Figure 5b indicated that IrO_x/MnO_x and $IrRuO_x/MnO_x$ resulted in lower ohmic resistances compared to the benchmark, possibly related to differences in the catalyst layer thickness, with $IrRuO_x/MnO_x$ showing somewhat lower HFR values compared to IrO_x/MnO_x, consistent with previous conductivity measurements (Figure 3d). To assess the effect of Ru dissolution, a constant cell current measurement was performed at 2 Acm^{-2} for $IrRuO_x/MnO_x$ (0.37 mg_{Ir+Ru} cm^{-2}) (Figure 5c, initial polarization curves are shown in Figure S25, Supporting Information). The measurement using IrO_x/MnO_x is shown in Figures S26 and S27a (Supporting Information). After 100 h, the cell voltage in Figure 5c showed negligible change, indicating that the identical Ru dissolution (Figure 3e) and structural changes (see Figure 4d) did not lead to rapid catalyst degradation. Although the restart after 100 h causes a slight increase in cell voltage, the voltage remains stable throughout the 150 h test. A 60 h cell test of $IrRuO_x/MnO_x$ with loading of 0.20 mg_{Ir+Ru} cm^{-2} was performed, as shown in Figures S25 and S27b (Supporting Information). Stable cell performance is achieved even with an ultralow loading. After 150 h of stability testing, the SEM image of $IrRuO_x/MnO_x$ showed a porous catalyst layer, consistent with the structures observed in the STEM images of

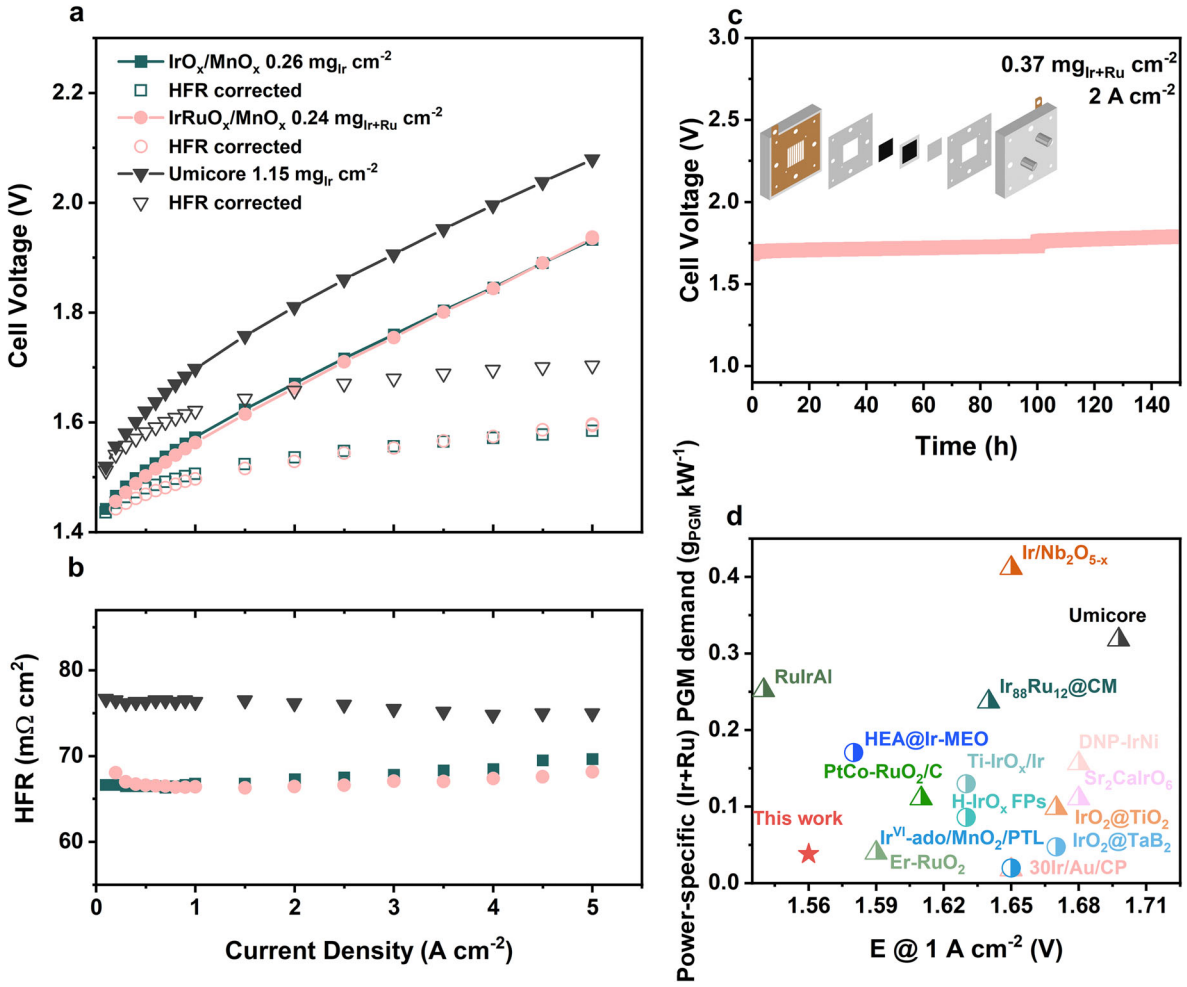

Figure 5. PEMWE performance of IrO_x/MnO_x and $IrRuO_x/MnO_x$ versus the benchmark catalyst. a) PEMWE polarization curves of IrO_x/MnO_x (green) and $IrRuO_x/MnO_x$ (pink) with (open) and without (closed) HFR correction. b) Corresponding HFR values of (a). c) Chronopotentiometric measurement of $IrRuO_x/MnO_x$ with an (Ir + Ru) loading of 0.37 mg cm^{-2} at 2 A cm^{-2}. (d) Comparison of power specific (Ir + Ru) demand at 70% LHV and cell voltage at 1 A cm^{-2} of $IrRuO_x/MnO_x$ (this work) with recently reported catalysts (see Table S9, Supporting Information). MEA specifications: Nafion NR212 membrane, 5 cm^2, decal transfer process; cathode catalyst loading of 0.1 mg_{Pt} cm^{-2}.

the as-prepared catalyst (Figure S28, Supporting Information). Some particle aggregation is present in the catalyst layer, which may influence its performance. Figure 5d puts the outstanding performance of $IrRuO_x/MnO_x$ into perspective compared to prior work using technologically relevant design parameters: It compares the power-specific (Ir + Ru) PGM demand (g_{PGM} kW^{-1}) at 70% LHV (≈1.79 V) and cell voltage at 1 A cm^{-2} of $IrRuO_x/MnO_x$ with those of recently reported catalysts (Table S9, Supporting Information). The $IrRuO_x/MnO_x$ achieved a power-specific (Ir + Ru) demand of 0.038 g_{PGM} kW^{-1} with an ultralow cell voltage of 1.56 V at 1 A cm^{-2}, which surpassed the technical target of 0.05 g_{PGM} kW^{-1}. The benchmark catalyst showed a value of 0.32 g_{PGM} kW^{-1} with a cell voltage of 1.69 V. The cell voltage at 2 A cm^{-2} is 1.66 V for $IrRuO_x/MnO_x$ and 1.67 V for IrO_x/MnO_x, which is outstanding compared to previous published values (Table S9 and Figure S29, Supporting Information). Overall, while IrO_x/MnO_x and $IrRuO_x/MnO_x$ exhibit distinct properties and OER performance in cell tests, both demonstrate excellent activity in MEA tests with only minor differences in performance. Both catalysts meet the 2035 target for PEMWEs, showing their potential for industrial application.

3. Conclusion

We have reported MnO_x-supported IrO_x and $IrRuO_x$ OER catalysts prepared using an aqueous scalable ion-exchange method. These two catalysts demonstrated distinct metal dissolution patterns and structural rearrangement under OER conditions as revealed by in situ FT-EXAFS and SFC-ICP-MS. While surface reconstruction in $IrRuO_x/MnO_x$ revealed a superior OER performance over IrO_x/MnO_x in RDE tests, no significant differences in MEA performance could be observed. An ultralow cell voltage of 1.66 V at 2 A cm^{-2} was achieved with $IrRuO_x/MnO_x$ and the power-specific (Ir + Ru) demands of both catalysts were below the 2035 target for PEMWEs. Long-term stability tests of PEMWE cells using $IrRuO_x/MnO_x$ reveal no significant performance degradation.

Supporting Information

Supporting Information is available from the Wiley Online Library or from the author.

Acknowledgements

Financial support by the Federal Ministry of Education and Research (Bundesministerium für Bildung und Forschung, BMBF) in the collaborative research project H_2Giga (project number: 03HY108D and 03HY108A) is gratefully acknowledged by the authors. The authors thankfully acknowledge financial support from the German Research Foundation (Deutsche Forschungsgemeinschaft, DFG) under grant STR-596/21-1. STEM Analysis is funded by DFG under the research project DFG-INST 131/789-1 FUGG (project number: 403371556). J.S. acknowledges support from the Cluster of Excellence "UniSysCat" funded by DFG under EXC2008-390540038.The authors thank the Center for Electron Microscopy (ZELMI) at TU Berlin in the context of the Alliance Center Electron Microscopy (ACEM) for support in the acquisition (and analysis) of the data. The ACEM was funded under the Excellence Strategy of the Federal Government and the Länder by the Berlin University Alliance (BUA). The authors thank Matthias Kroschel, Jiasheng Lu, Jingyi Wang, and An Guo, (Technische Universität Berlin), for contributing to data collection at the synchrotron radiation sources. The authors thank the beam scientists Dr. Michael Haumann and Dr. Götz Schuck as well as the beamline KMC-3 XPP of BESSY II, Berlin, respectively.

Open access funding enabled and organized by Projekt DEAL.

Conflict of Interest

The authors declare no conflict of interest.

Data Availability Statement

The data that support the findings of this study are available from the corresponding author upon reasonable request.

Keywords

electrocatalysis, electrolysis, iridium, oxygen evolution reaction, PEM water electrolyzer

Received: December 6, 2024
Revised: February 25, 2025
Published online: March 19, 2025

[1] a) C. W. Lee, J. Zhong, *Renew. Sustain. Energy Rev.* **2015**, *51*, 288; b) I. Gunnarsdottir, B. Davidsdottir, E. Worrell, S. Sigurgeirsdottir, *Renew. Sustain. Energy Rev.* **2020**, *133*, 110294.

[2] a) M. A. Pellow, C. J. M. Emmott, C. J. Barnhart, S. M. Benson, *Energy Environ. Sci.* **2015**, *8*, 1938; b) T. M. Gür, *Energy Environ. Sci.* **2018**, *11*, 2696.

[3] M. A. Rosen, S. Koohi-Fayegh, *Energy Eco. Environ.* **2016**, *1*, 10.

[4] M. Clapp, C. M. Zalitis, M. Ryan, *Catal. Today* **2023**, *420*, 114140.

[5] H. Wang, Z. Yan, F. Cheng, J. Chen, *Adv. Sci.* **2024**, *11*, 2401652.

[6] a) S. Siracusano, N. Van Dijk, E. Payne-Johnson, V. Baglio, A. S. Aricò, *Appl. Catal., B* **2015**, *164*, 488; b) K. Qin, H. Yu, W. Zhu, Y. Zhou, Z. Guo, Q. Shao, Y. Wu, X. Wang, Y. Li, Y. Ji, F. Liao, Y. Liu, Z. Kang, M. Shao, *Adv. Funct. Mater.* **2024**, 2402226; c) K. Sardar, E. Petrucco, C. I. Hiley, J. D. B. Sharman, P. P. Wells, A. E. Russell, R. J. Kashtiban, J. Sloan, R. I. Walton, *Angew. Chem., Int. Ed.* **2014**, *53*, 10960; d) W. Zhu, X. Song, F. Liao, H. Huang, Q. Shao, K. Feng, Y. Zhou, M. Ma, J. Wu, H. Yang, H. Yang, M. Wang, J. Shi, J. Zhong, T. Cheng, M. Shao, Y. Liu, Z. Kang, *Nat. Commun.* **2023**, *14*, 5365.

[7] a) R. V. Genova-Koleva, F. Alcaide, G. Álvarez, P. L. Cabot, H.-J. Grande, M. V. Martínez-Huerta, O. Miguel, *J. Energy Chem.* **2019**, *34*, 227; b) A. Martínez-Séptimo, M. A. Valenzuela, P. Del Angel, R. d. G. González-Huerta, *Int. J. Hydrogen Energy* **2021**, *46*, 25918; c) J. Xu, J. Li, Z. Lian, A. Araujo, Y. Li, B. Wei, Z. Yu, O. Bondarchuk, I. Amorim, V. Tileli, B. Li, L. Liu, *ACS Catal.* **2021**, *11*, 3402; d) X. Li, Z. Gu, J. Cheng, G. Zhang, F. Zheng, J. Huang, J. Xu, G. Wei, J. Zhang, *ACS Appl. Nano Mater.* **2024**, *7*, 12958; e) Y. Liu, M. Zhang, C. Zhang, H. Zhang, H. Wang, *Nanoscale* **2024**, *16*, 9382; f) J. Li, Z. Lian, Q. Li, Z. Wang, L. Liu, F. L. Deepak, Y. Liu, B. Li, J. Xu, Z. Chen, *Nano Res.* **2022**, *15*, 5933.

[8] a) A. Li, H. Ooka, N. Bonnet, T. Hayashi, Y. Sun, Q. Jiang, C. Li, H. Han, R. Nakamura, *Angew. Chem., Int. Ed.* **2019**, *58*, 5054; b) Y. Zhou, F. Chen, R. Tian, S. Huang, R. Chen, M. Li, T. Wan, Z. Han, D. Wang, D. Chu, *Surf. Interfaces* **2021**, *26*, 101398; c) Y.-R. Z. Zhenbin Wang, I. Chorkendorff, J. K. Nørskov, *ACS Energy Lett.* **2020**, *5*, 2905; d) A. Erbe, M. F. Tesch, O. Rüdiger, B. Kaiser, S. DeBeer, M. Rabe, *Phys. Chem. Chem. Phys.* **2023**, *25*, 26958.

[9] Y. He, Z. Kang, J. Li, Y. Li, X. Tian, *Ind. Chem. Mater.* **2023**, *1*, 312.

[10] a) S. Zhang, X. Ma, Y. He, Y. Zhu, Z. Wang, *Int. J. Hydrogen Energy* **2023**, *48*, 10532; b) S. D. Ghadge, O. I. Velikokhatnyi, M. K. Datta, P. M. Shanthi, S. Tan, K. Damodaran, P. N. Kumta, *ACS Catal.* **2019**, *9*, 2134.

[11] a) H. Luo, F. Lin, Q. Zhang, D. Wang, K. Wang, L. Gu, M. Luo, F. Lv, S. Guo, *J. Am. Chem. Soc.* **2024**, *146*, 19327; b) C. Lin, J.-L. Li, X. Li, S. Yang, W. Luo, Y. Zhang, S.-H. Kim, D.-H. Kim, S. S. Shinde, Y.-F. Li, Z.-P. Liu, Z. Jiang, J.-H. Lee, *Nat. Catal.* **2021**, *4*, 1012; c) Y. Zeng, L. Yan, S. Tian, X. Sun, *ACS Appl. Mater. Interfaces* **2023**, *15*, 47103; d) L. Quan, Y. Cao, J. Liu, B. Y. Xia, X. Zhao, B. You, *J. Mater. Chem. A* **2024**, *12*, 19958.

[12] a) T. Smolinka, N. Wiebe, P. Sterchele, A. Palzer, F. Lehner, M. Jansen, S. Kiemel, R. Miehe, S. Wahren, F. Zimmermann, *Studie IndWEDe. Industrialisierung der Wasserelektrolyse in Deutschland*, Fraunhofer-Gesellschaft, Munich, Germany **2018**; b) C. Minke, M. Suermann, B. Bensmann, R. Hanke-Rauschenbach, *Int. J. Hydrogen Energy* **2021**, *46*, 23581.

[13] J. Li, F. L. Deepak, *Chem. Rev.* **2022**, *122*, 16911.

[14] A. Kozawa, *J. Electrochem. Soc.* **1959**, *106*, 552.

[15] M. Bernt, C. Schramm, J. Schröter, C. Gebauer, J. Byrknes, C. Eickes, H. A. Gasteiger, *J. Electrochem. Soc.* **2021**, *168*, 084513.

[16] M. Zlatar, D. Nater, D. Escalera-López, R. M. Joy, P. Pobedinskas, K. Haenen, C. Copéret, S. Cherevko, *Electrochim. Acta* **2023**, *444*, 141982.

[17] S. Geiger, O. Kasian, M. Ledendecker, E. Pizzutilo, A. M. Mingers, W. T. Fu, O. Diaz-Morales, Z. Li, T. Oellers, L. Fruchter, A. Ludwig, K. J. J. Mayrhofer, M. T. M. Koper, S. Cherevko, *Nat. Catal.* **2018**, *1*, 508.

[18] a) A. Zagalskaya, V. Alexandrov, *ACS Catal.* **2020**, *10*, 3650; b) D. Escalera-López, S. Czioska, J. Geppert, A. Boubnov, P. Röse, E. Saraçi, U. Krewer, J.-D. Grunwaldt, S. Cherevko, *ACS Catal.* **2021**, *11*, 9300.

[19] S. Czioska, A. Boubnov, D. Escalera-López, J. Geppert, A. Zagalskaya, P. Röse, E. Saraçi, V. Alexandrov, U. Krewer, S. Cherevko, J.-D. Grunwaldt, *ACS Catal.* **2021**, *11*, 10043.

[20] L. Yao, F. Zhang, S. Yang, H. Zhang, Y. Li, C. Yang, H. Yang, Q. Cheng, *Adv. Mater.* **2024**, *36*, 2314049.

[21] S. C. Daniel Escalera-López, J. Geppert, A. Boubnov, P. Röse, E. Saraçi, U. Krewer, J.-D. Grunwaldt, S. Cherevko, *ACS Catal.* **2021**, *11*, 9300.